ADVANCED ELECTRONIC MATERIALS
www.advelectronicmat.de

Stable Al_2O_3 Encapsulation of MoS_2-FETs Enabled by CVD Grown h-BN

Agata Piacentini, Damiano Marian, Daniel S. Schneider, Enrique González Marín, Zhenyu Wang, Martin Otto, Bárbara Canto, Aleksandra Radenovic, Andras Kis, Gianluca Fiori, Max C. Lemme, and Daniel Neumaier**

Molybdenum disulfide (MoS_2) has great potential as a two-dimensional semiconductor for electronic and optoelectronic application, but its high sensitivity to environmental adsorbents and charge transfer from neighboring dielectrics can lead to device variability and instability. Aluminum oxide (Al_2O_3) is widely used as an encapsulation layer in (opto)-electronics, but it leads to detrimental charge transfer n-doping to MoS_2. Here, this work reports a scalable encapsulation approach for MoS_2 field-effect transistors (FETs) where hexagonal boron nitride (h-BN) monolayers are employed as a barrier layer in-between each of the Al_2O_3 and MoS_2 interfaces. These devices exhibit a significant reduction of charge transfer, when compared to structures without h-BN. This benefit of h-BN in the gate stack is confirmed by ab initio density functional theory calculations. In addition, the devices with h-BN layers show very low hysteresis even under ambient operating conditions.

1. Introduction

2D materials have attracted massive attention especially for their potential as post-silicon channel material in ultrascaled field-effect transistor (FET) or for flexible electronic applications.[1] Graphene was the first 2D material to be employed as FET channel,[2,3] but due to its lack of band gap, graphene is not suited for logic applications. Research has not stopped here, but in the past decade, many other graphene-like ultrathin 2D nanomaterials with a sufficiently large band gap, such as transition metal dichalcogenides (TMDs),[4,5] and black phosphorus were explored in FETs technology.[6] Among them, particular attention was given to TMDs for their semiconducting properties. So far, MoS_2 is the most widely studied TMD because of its rather high carrier mobility compared to ultrathin silicon FETs and its specific optoelectronic properties.[7–10] Great effort was made to improve the performances of MoS_2 electronic devices,[11–14] however, the material is strongly affected by the measurement environment and dielectric interfaces, often leading to large hysteresis in MoS_2-based devices.[15] While low hysteresis has been demonstrated under ambient conditions for FETs made from exfoliated MoS_2 flakes,[14,16,17] the same was achieved only under vacuum conditions for FETs made from chemical vapor deposited (CVD) grown material.[11,18] Hysteresis in MoS_2-based FETs is attributed to charge transfer from defect states in the gate dielectric, interface states, and from neighboring adsorbates such as O_2 and H_2O coming from the moisture in the air.[19] The latter problem is the predominant effect under ambient

A. Piacentini, D. S. Schneider, M. Otto, B. Canto, M. C. Lemme, D. Neumaier
Advanced Microelectronic Center Aachen (AMICA)
AMO GmbH
Otto-Blumenthal-Straße 25, 52074 Aachen, Germany
E-mail: piacentini@amo.de

A. Piacentini, D. S. Schneider, M. C. Lemme
Chair of Electronic Devices
RWTH Aachen University
Otto-Blumenthal-Straße 2, 52074 Aachen, Germany

The ORCID identification number(s) for the author(s) of this article can be found under https://doi.org/10.1002/aelm.202200123.

DOI: 10.1002/aelm.202200123

D. Marian, G. Fiori
Dipartimento di Ingegneria dell'Informazione
Università di Pisa
Via Girolamo Caruso 16, Pisa 56122, Italy

E. González Marín
Department of Electronics and Computer Technology
University of Granada
Avenida de la Fuente Nueva S/N, Granada 18071, Spain

Z. Wang, A. Kis
Electrical Engineering Institute
École Polytechnique Fédérale de Lausanne (EPFL)
Lausanne 1015, Switzerland

B. Canto, D. Neumaier
School of Electrical, Information and Media Engineering
Bergische Universität Wuppertal
Lise-Meitner-Straße 13, 42119 Wuppertal, Germany
E-mail: dneumaier@uni-wuppertal.de

A. Radenovic
Intitute Biotechnology
École Polytechnique Fédérale de Lausanne (EPFL)
Lausanne 1015, Switzerland

condition and various encapsulation methods have been reported in literature to improve the MoS_2 protection from the external environment.[16,20,21] The most common passivation method is the deposition of dielectric material on top of the channel, which ideally would ultimately also serve as a gate dielectric. In particular, atomic layer deposition (ALD) of Al_2O_3 is a common encapsulation layer, which is also used as the moisture barrier in organic light emitting diodes.[22,23] However, it is known that this high-k dielectric retains fixed charges with positive polarity, which can capture electrons and change the threshold voltage of FETs via electrostatic doping of the MoS_2 layer.[21,24–26] This effect is visible in the transfer characteristic of the FETs. After the dielectric deposition on-top of MoS_2, the transfer characteristic curve is shifted toward negative gate voltages, which is a confirmation of the encapsulation induced n-type doping.[11,13,24–27] Another strategy for the encapsulation of MoS_2 FETs is using hexagonal boron nitride (h-BN).[16,28–31] This approach has been studied using exfoliated materials, however there are few reports using scalable, CVD-grown films. Thick micromechanical exfoliated h-BN flakes have been employed as a gate dielectric, and they show predominantly van der Waals interaction with 2D materials due to the layered nature.[16,28,32,33] Nevertheless, because of its relatively small band gap and low dielectric constant it is not the ideal material for this purpose alone.[15,34,35] In alternative, flakes of h-BN were exploited as a barrier layer in between silicon dioxide (SiO_2) and MoS_2 flakes.[16,28,30,36,37] Here, h-BN was shown to minimize the charge trapping from the SiO_2 dielectric due to a screening effect, which leads to a near-zero hysteresis in the transistor characteristics. h-BN encapsulated devices show excellent interface quality, but exfoliated materials do not represent a scalable process. In this work, we propose a scalable encapsulation of MoS_2 by Al_2O_3 using a monolayer of h-BN as an interfacial layer between the MoS_2 and the Al_2O_3. This h-BN/MoS_2/h-BN heterostructure reduces n-doping caused by the Al_2O_3 encapsulation. This is confirmed by ab initio density functional theory calculations. Moreover, we observe a reduction of the hysteresis for ultraslow sweeping time, which can be attributed to an improved dielectric interface.

2. Results and Discussion

MoS_2-based FETs in local-back-gate configuration using ALD deposited Al_2O_3 as gate dielectric layer were studied. The device schematic is represented in **Figure 1**a. The channel material was monolayer MoS_2 grown by metal-organic chemical vapor deposition (MOCVD), sandwiched between two monolayers of CVD-grown h-BN fabricated through wet transfer. The h-BN/MoS_2/h-BN stack is then encapsulated with ALD Al_2O_3. A schematic of the stack is represented in Figure 1c. For simplicity, we refer to this stack structure as MBN-FET. In parallel, identical devices but without the two h-BN layers were fabricated as reference, and referred to as M-FET. The device and stack structure are in Figure 1b,d, respectively. The detailed fabrication process is described in the Experimental Section, while optical images of the devices are in Figure 1e,f.

Confocal Raman and photoluminescence (PL) measurements were performed on the two stacks before and after the final encapsulation with 40 nm Al_2O_3. **Figure 2**a,b shows Raman and PL spectra for the M-FET stack and MBN-FET stack in blue and red, respectively. Two-dimensional MoS_2 has two detectable vibrational modes in Raman spectroscopy: The in-plane E_{2g} mode generated from opposite vibration of two S atoms with respect to the Mo atom and the A_{1g} mode resulted from the out-of-plane vibration of S atoms in the opposite directions.[38,39] The two vibrational modes are visible in Figure 2a and remain unaltered for both stacks before and after the Al_2O_3 encapsulation layer (solid and dashed lines, respectively), i.e., the vibrational modes are not affected by the Al_2O_3 top encapsulation. This is in line with previous literature results, where the Raman peaks remained unaltered after Al_2O_3 encapsulation.[21,40] The M-FET has a wavenumber difference of 17 cm^{-1} between A_{1g} (≈400 cm^{-1}) and E_{2g} (≈383 cm^{-1}) peaks which confirms the monolayer nature of the MoS_2. A_{1g} mode of the MBN-FET

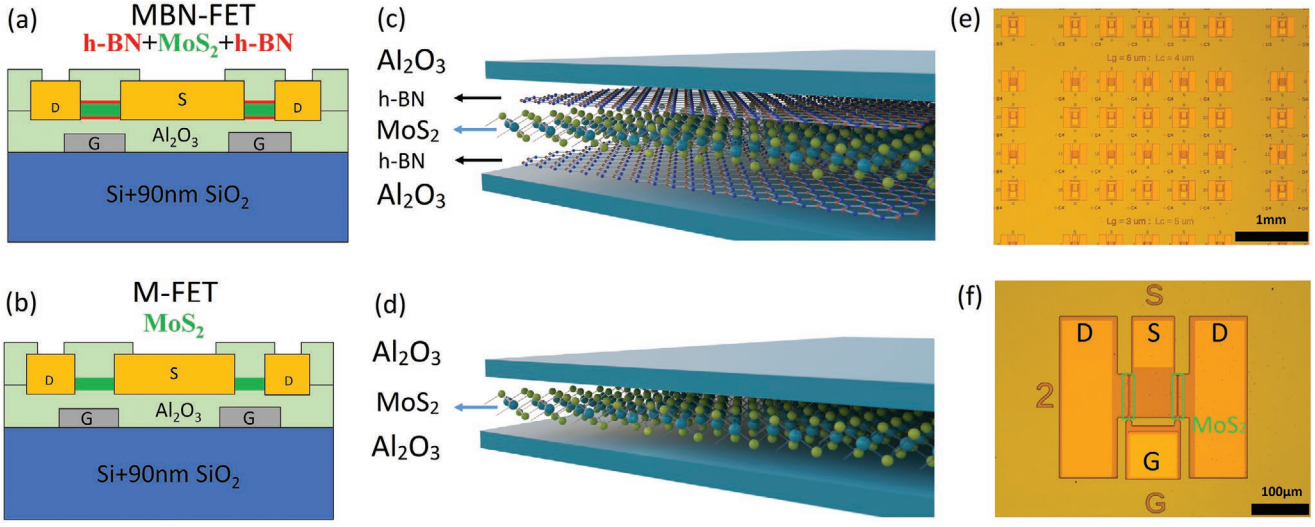

Figure 1. Cross-section schematic of the device structure and the channel material stack for MBN-FETs (a,c) and M-FETs (b,d), respectively. e) Optical images of part of the sample and f) magnification of one structure. Source (S), drain (D), and gate (G) electrodes, as well as the MoS_2 channel are labeled.

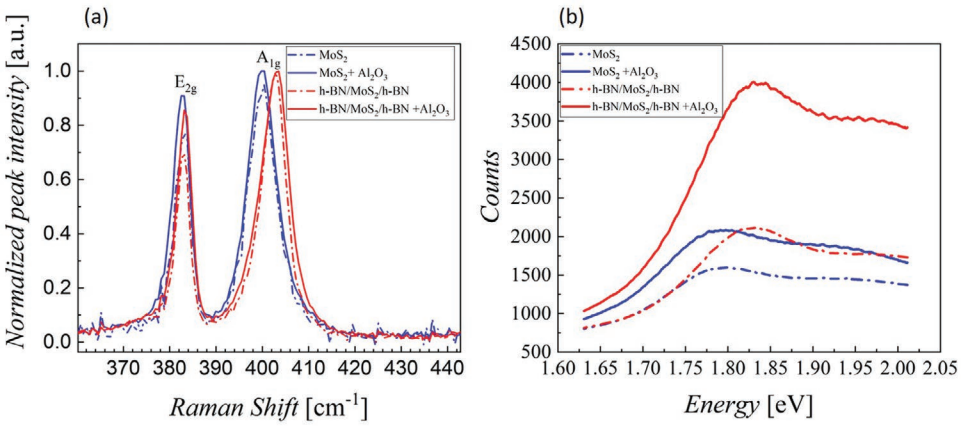

Figure 2. a) Raman spectra, and b) photoluminescence (PL) data for MBN-FETs in red and M-FETs in blue. The measurements were conducted before (solid lines) and after (dashed lines) the top Al_2O_3 encapsulation.

is blue-shifted with respect to the M-FET. In the MBN-FET case, the wavenumber difference is increased to 19.5 cm^{-1} (A_{1g} ≈402.5 cm^{-1} and E_{2g} ≈383 cm^{-1}). However, because the MoS_2 consisted of the very same monolayer as for the M-FET, the higher difference between the peaks can be interpreted as a stiffening of the vibrational mode, attributed to the van der Waals interactions between MoS_2 and h-BN.[29,41] This behavior is similar to that of MoS_2 multilayers, where the multiple layers suppress the out-of-plane vibrational mode. Hence, the present result is an indication of stronger van der Waals interaction between h-BN and MoS_2 while the interaction between Al_2O_3 and MoS_2 is significantly weaker due to large densities of dangling bonds and impurities at the interface.[32,35,42,43] The influence of surrounding medium on Raman and PL measurement of monolayer MoS_2 was previously investigated in many reports.[44–46] The A_{1g} Raman shift was attributed to a doping effect of the substrate, while E_{2g} is barely affected by the substrate. A stiffening of the A_{1g} is associated to a reduction of electron density, and this is in agreement with the expectation that MBN stack has lower charges impurities due to the screening effect of h-BN when compared to M stack.[44,47] The PL data in Figure 2b exhibits lower intensity as well as red shifts of the peaks in the case of the M-FET with respect to MBN-FET. The former can be attributed to doping in the monolayer MoS_2: depending on the carrier density in the material, the PL is known to switch between exciton and trion recombination.[48,49] The quenching of the PL intensity peak in the M-FET (blue curve) originates in the suppression of the natural excitons in favor of the formation of negative trions by accepting an electron. The trion recombination becomes the dominant effect and it happens at lower energy which can explain the red shift of the peak. The effect has been attributed particularly to n-doping in MoS_2 due to the positive fixed charges in Al_2O_3 encapsulation, which causes electrostatic doping in the channel.[49] Hence, the PL measurements indicate that h-BN can suppress the n-type doping and this is in accordance with the previous Raman results in Figure 2a.

Detailed electric characterizations of field effect transistors were performed in order to study electrically the impact of the h-BN layers on the doping level, interfacial charge traps, and carrier mobility. **Figure 3**a,c displays the transfer characteristics measured at a fixed source-drain voltage of V_{ds} = 1 V for one MBN-FET and one M-FET, respectively. The blue curve in both cases represents the transfer characteristics in ambient before the Al_2O_3 top encapsulation, whereas the red curve shows the electrical response after the encapsulation. Before the encapsulation, the transfer characteristic was also measured in vacuum (orange lines in Figure 3a,c). Figure 3b,d reports the corresponding output characteristics at different V_g of the two FETs. The transfer characteristics for the MBN-FET before and after the Al_2O_3 encapsulation (Figure 3a) show an excellent overlap of the two curves: the threshold voltage of the device (V_{TH}), the subthreshold swing (SS), the field-effect mobility (μ), and the on-off ratio (I_{on}/I_{off}) of the device remain almost unchanged after the encapsulation process. Corresponding values are: V_{TH} = 0.6 and 0.5 V, SS = 243 and 245 mV dec^{-1}, μ = 6 and 7 $cm^2\ V^{-1}\ s^{-1}$, and I_{on}/I_{off} close to 10^7, where the first number represents the values before encapsulation and the second the values after encapsulation. In contrast, for the M-FET case (Figure 3c), there is an evident shift of the curve toward more negative gate voltages after the Al_2O_3 deposition which translates to a shift of the threshold voltage. The transistor is still able to turn off completely, but at significantly higher negative gate voltage (Figure S1, Supporting Information). This is an indication of an n-doping effect after the deposition of the Al_2O_3 passivation layer and it is in accordance with the PL measurements and the literature results where this phenomenon is attributed to the positive fixed charges that Al_2O_3 brings to the MoS_2. The bottom Al_2O_3 layer seems not to affect the threshold voltage as much as the top layer. MoS_2 is transferred to the substrate in ambient condition where the presence of residuals could lead to an increase of the distance between the layers leading to a weaker interaction. As it will be shown by DFT simulation later (Figure 6c) the distance between Al_2O_3 and MoS_2 is a key parameter to determine the strength of the charge transfer. However, we note that an interpretation of the data before encapsulation is rather complex, as also the uncovered or h-BN covered top surface has an impact on the threshold voltage even under vacuum conditions. The relevant parameters of the M-FET device before/after the encapsulation are: V_{TH} = 0.3 and −0.7 V, SS = 273 and 294 mV dec^{-1}, μ = 7 and 8 $cm^2\ V^{-1}\ s^{-1}$, and I_{on}/I_{off} close to 10^7. Another noticeable difference in the two types of devices is the hysteresis. The MBN-FET transfer curves show a significantly higher overlap between the curve in forward and

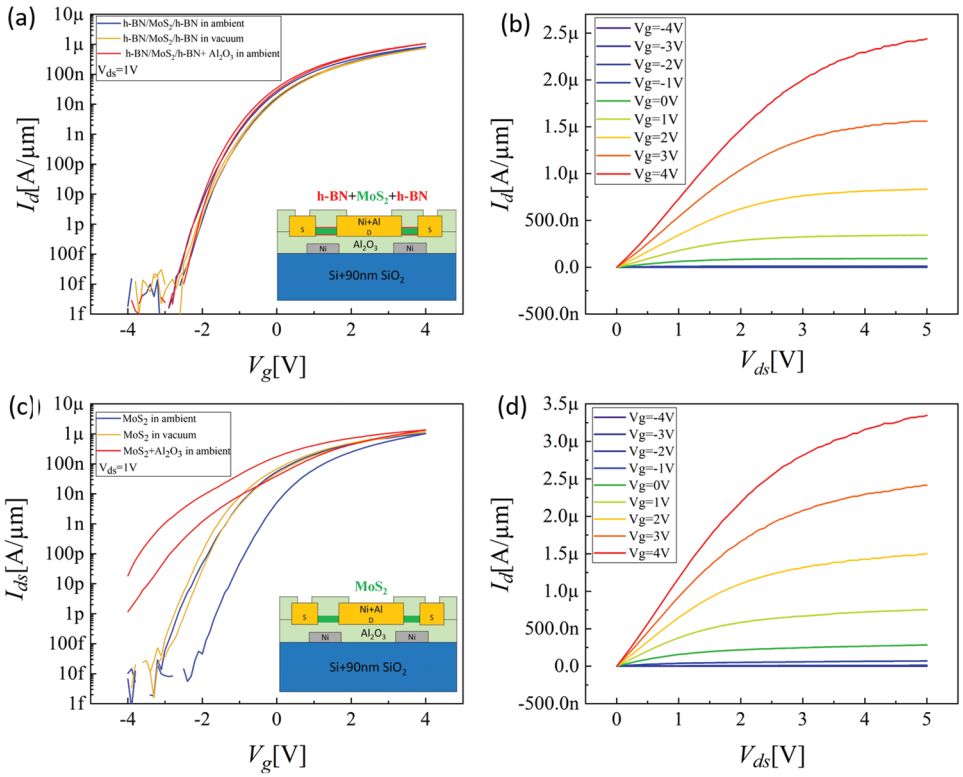

Figure 3. Electrical characterization of an MBN-FET and an M-FET. a) Transfer characteristics of an MBN-FET before encapsulation in ambient (blue), in vacuum (yellow), and after encapsulation (red). Low hysteresis and low V_{TH} variation are observed in all conditions. b) Corresponding output characteristics of the encapsulated device. c) Transfer characteristics of an M-FET in the three different conditions. High hysteresis and an n-doping shift of the transfer curve is observed after the Al_2O_3 encapsulation. d) Corresponding output characteristics of the encapsulated device.

reverse sweep mode with respect to the M-FET. In MoS_2 based FETs, hysteresis is mainly caused by charge trapping and two main factors are charge transfer at the interface between MoS_2 and the Al_2O_3 and from adsorbates in the air.[19] Lower hysteresis of the MBN-FET indicates that h-BN layers improve the interface quality with the dielectric and also prevent the adsorption of atmospheric molecules especially before encapsulation. The hysteresis variation in the case of M-FETs in ambient and vacuum condition conforms the latter (yellow curve in Figure 3a,c), as it is more pronounced than for the MBN-FET.

We have measured a total of 27 MBN-FETs and 27 M-FETs to verify the reproducibility of the results. **Figure 4**a,b shows $I_d - V_g$ curves of the MBN-FETs before and after the Al_2O_3 deposition, respectively, while Figure 4c,d reports the results for the M-FETs (these measurements were conducted in ambient condition). Again, it is clearly visible that the n-doping shift is reduced for all MBN-FETs compared to the M-FETs, where the MoS_2 is in direct contact with Al_2O_3. The key parameters ΔV_{TH}, hysteresis and SS are summarized in **Figure 5**a–c. Figure 5a shows the statistics of threshold voltage shifts (ΔV_{TH}) extracted in the forward sweep before and after the Al_2O_3 encapsulation for the 27 M-FETs and MBN-FETs. The extraction method for V_{TH} is shown in the Supporting Information (Section S2, Supporting Information), where it is shown that the minimum ΔV_{TH} measurable is equivalent to the minimum gate voltage step used in the measurements (in this case 100 mV, underlined with a dashed red line). Figure 5b collects the statistics of hysteresis for all the devices. Here, the hysteresis is calculated as the difference in the threshold voltage in backward and forward sweeping, and the dashed red line indicates the minimum measurable value. ΔV_{TH} and hysteresis are on average lower in the case of the MBN-FETs which demonstrate the beneficial effect of h-BN in the electrical performances of MoS_2-FETs by reducing charge traps at the interfaces. Statistics of SS of the FETs at different stages are shown in Figure 5c. While the SS values before the Al_2O_3 deposition of the two device typologies are comparable, a clear increase of the SS range is visible for M-FETs after the Al_2O_3 encapsulation. Note that in this case, the SS is overestimated because the voltage range of the $I_d - V_g$ curves does not cover the full subthreshold regime, and the SS is extracted close to V_{TH}. In the Supporting Information (Section S1, Supporting Information), a complete voltage sweep of an M-FET after the Al_2O_3 is reported, and it is evident that the SS increases for the M-FET. In the case of MBN-FETs, SS values before and after the deposition of Al_2O_3 are similar. Also, the mobility is similar for both types of devices and slightly increases after encapsulation (see Figure S3, Supporting Information).

In order to rationalize the n-do ping of the MoS_2 channel due to the Al_2O_3 encapsulation, we have performed density functional theory calculations using the Quantum Espresso package.[50] In particular, the focus was on the structures reported in **Figure 6**a,b, before and after the Al_2O_3 encapsulation in correspondence with the device structure of the M-FETs

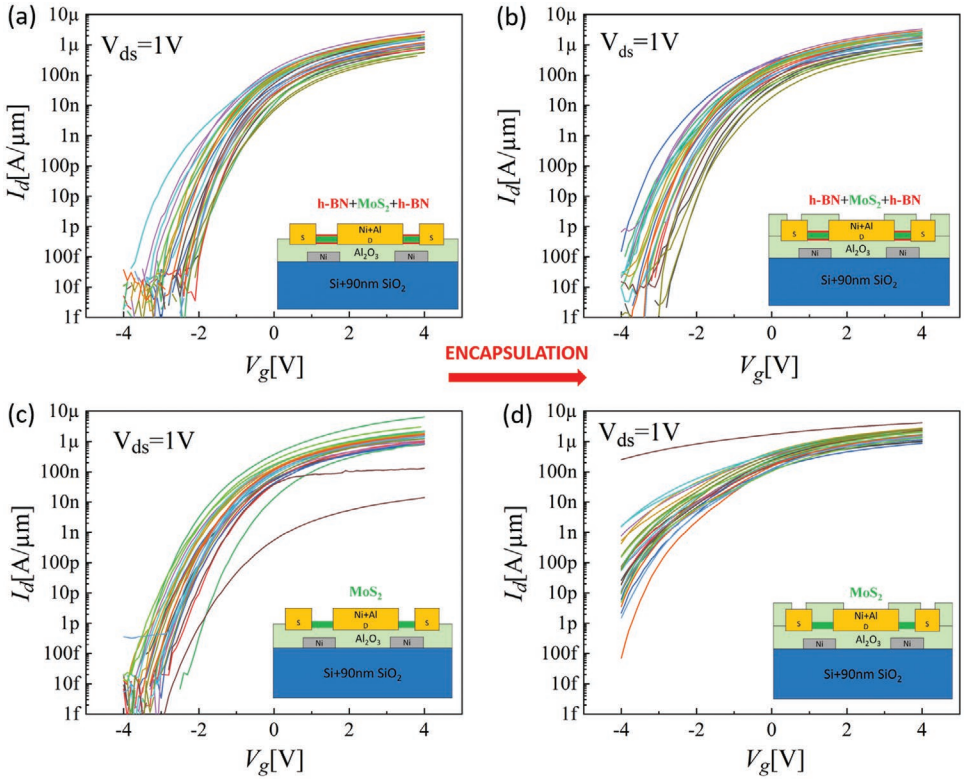

Figure 4. Transfer characteristics measured on 27 MBN-FETs (a) and on 27 M-FETs (b), before encapsulation. Transfer characteristics measured on the same devices after encapsulation, (c and d), respectively. Inset: schematics of the corresponding device fabrication stages.

and MBN-FETs, respectively. Details of the calculations are reported in the Experimental Section, while additional material about the simulated structures is reported in the Supporting Information (Section S5, Supporting Information). First, we have performed an optimization of the structures, leading to an equilibrium distance between both Al_2O_3 slabs of $d_0 = 8.48$ Å for the M-FETs while $d_0 = 15.79$ Å for the MBN -FETs. The distance between the h-BN and the MoS_2 layer in the latter is d_{hBN} = 3.42 Å. The charge transfer from the Al_2O_3 to the MoS_2 layer in both stacks before and after the encapsulation was determined using the Bader formalism.[51] In particular, the charge transfer due to the addition of an encapsulating layer of Al_2O_3 to an Al_2O_3/MoS_2 and an Al_2O_3/h-BN/MoS_2/h-BN structure has been calculated. Two different interfaces of Al_2O_3 were studied and the mean charge transfer due to each Al_2O_3 termination was obtained (see Section S6, Supporting Information, for more details). For the optimized distances d_0, a charge transfer of 2.96×10^{12} carriers cm^{-2} was obtained for the $Al_2O_3/MoS_2/Al_2O_3$ stack whereas 0.28×10^{12} carriers cm^{-2} was obtained for the Al_2O_3/h-BN/MoS_2/h-BN/Al_2O_3 stack. This corresponds to a reduction of an order of magnitude in charge carrier density when an h-BN monolayer is placed in between Al_2O_3 and

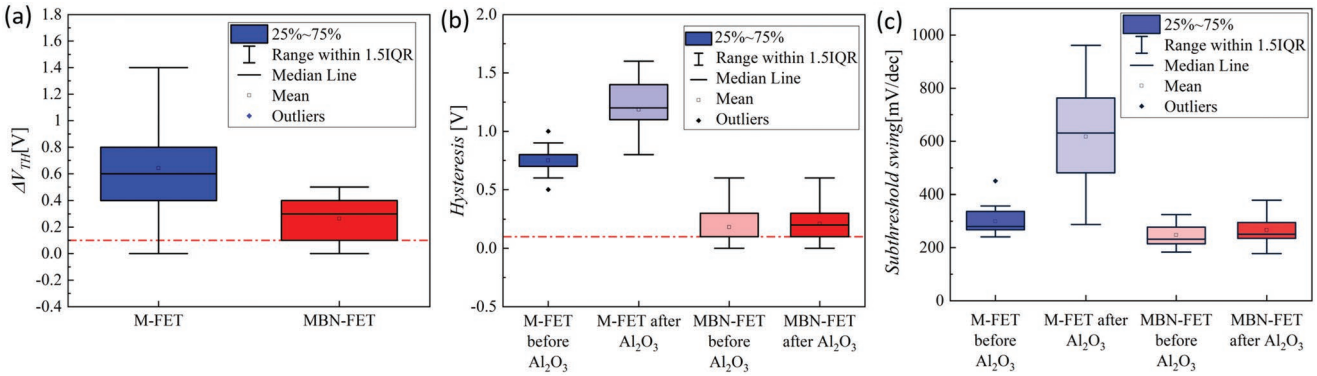

Figure 5. a) Statistical representation of V_{TH} shifts measured on the same device before and after the Al_2O_3 for all the M-FETs (blue) and MBN-FETs (red). This parameter quantifies the n-doping caused by the Al_2O_3 encapsulation. Statistical data of b) the hysteresis and c) of subthreshold swing (SS) measured for all the devices at the different encapsulation stages. MBN-FETs show higher stability in the electrical performance. The dashed lines in (a) and (b) indicate the minimum detectable values.

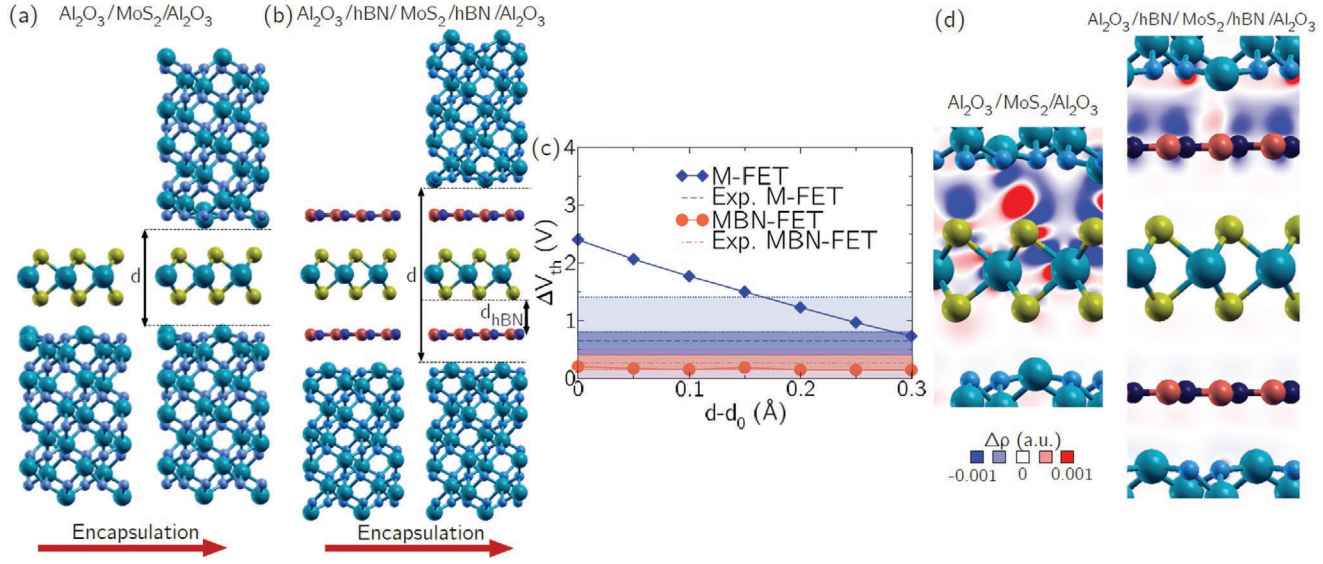

Figure 6. a) Al_2O_3/MoS_2 and b) Al_2O_3/h-BN/MoS_2/h-BN structure before and after the Al_2O_3 encapsulation. The distances d and d_{hBN} are indicated. c) ΔV_{TH} shift for different values of d–d_0 both for the M-FET (blue diamonds) and the MBN-FET (red circles) structures. With dashed and point-dashed lines we report the experimental mean value for the M-FET and the MBN-FET, respectively. Shaded regions indicate 25%–75% and the 1.5IQR ranges. d) Charge density difference calculated for the $Al_2O_3/MoS_2/Al_2O_3$ (left) and Al_2O_3/h-BN/MoS_2/h-BN/Al_2O_3 structures (right).

MoS_2. It is illustrative to analyze the charge density difference showing the redistribution of the charges due to the encapsulation for the two different structures: in Figure 6d it can be clearly observed that the addition of the top Al_2O_3 slab in the Al_2O_3/MoS_2 structure induces a significant rearrangement of the charges in the MoS_2 layer, while in the case of the Al_2O_3/h-BN/MoS_2/h-BN structure the MoS_2 is almost unaltered and the charge rearrangement is confined to the Al_2O_3/h-BN interface (see Section S6, Supporting Information, for more details). The charge transfer, which is likely due to the extended surface states of Al_2O_3, is thus clearly affected by the presence of h-BN which screens the interaction of these states with MoS_2.

The theoretically optimized distance between the MoS_2 and Al_2O_3 layers can be, in practice, affected by contaminations leading to larger interlayer distances and changing the MoS_2 n-doping. In order to assess this possibility, the charge transfer has been calculated varying the distance between the Al_2O_3 slabs (d), keeping d_{hBN} to its relaxed value in the Al_2O_3/h-BN/MoS_2/h-BN/Al_2O_3 structure for each d. The charge transfer is severely affected by the actual interlayer distance, as the overlapping of the extended surface states of Al_2O_3 with MoS_2 is reduced when the distance increases. We have then estimated the threshold voltage shift (ΔV_{TH}) due to the Al_2O_3 deposition in the FET devices in correspondence to the calculated charge transfer.

In Figure 6c, ΔV_{TH} is reported as a function of the distance between the Al_2O_3 layers: ΔV_{TH} which is directly proportional to the transferred charge, decreases as the distance between layers increases, and it does more significantly for the M-FET, from 2.4 V till 0.7 V, than for the MBN-FET, from 0.2 V till 0.14 V. Figure 6c shows also the mean values and the variability ranges of the experimental threshold voltage shift for both the M-FET and the MBN-FET: in the case of MBN-FET, the ΔV_{TH} is compatible with the experimental observation (and almost independent of the distance), while for the M-FET, ΔV_{TH} is in the range of the experimental values for $d - d_0 > 0.15$ Å reaching the mean value for $d - d_0 = 0.3$ Å.

Finally, we performed ultraslow sweep hysteresis measurement in vacuum condition with total sweep times (t_{sw}) of several thousands of seconds to verify the electrical stability. The increase in t_{sw} will allow slower traps to contribute to the hysteresis.[32] In **Figure 7**a, the $I_d - V_g$ characteristics measured for the two types of devices at short t_{sw} (30 s) and long t_{sw} (1750 s) are compared. The M-FETs (blue) show an evident higher hysteresis with respect to the MBN-FET (in red) both in short and long sweeping rate. In this case, the hysteresis was extracted in the subthreshold regime, and, to better compare the data, we normalized the hysteresis for the field factor $K = \Delta V_g/d_{ins}$ with ΔV_g being the width of the sweep voltage range and d_{ins} the insulator thickness.[18] In Figure 7b, the normalized hysteresis is plotted as a function of the inverse of the sweeping time: the MBN-FET hysteresis is smaller by almost one order of magnitude compared to that of the M-FETs at all frequencies ($1/t_{sw}$). This confirms higher interface quality of the MoS_2 with the surrounding Al_2O_3 dielectric layer with less defects and trap states. Noise measurements were also conducted and the results suggest a positive impact on the 1/f noise level in the devices with h-BN. However, further investigations are needed to fully understand the different contributions to the 1/f noise. Details on the 1/f noise measurements are available in Section S4 (Supporting Information).

3. Conclusion

We have demonstrated that a monolayer of h-BN at the interface of MOCVD grown MoS_2 and Al_2O_3 significantly reduces unintentional charge transfer and improves the interface

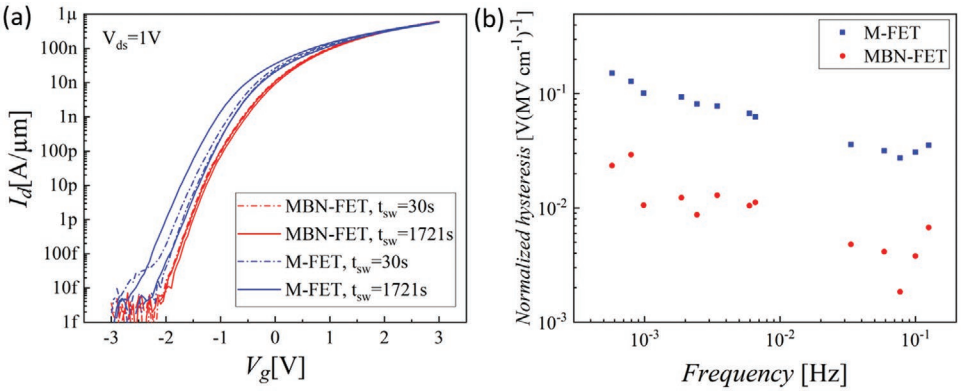

Figure 7. a) Stability measurement for an MBN-FET (red) and an M-FET (blue) at a short (dash line) and long (continuous line) sweeping speeds. b) Normalized hysteresis as a function of the sweep time for the two stacks. The MBN-FET shows one order of magnitude lower hysteresis with respect to the M-FET, which proves and improvement in the dielectric interface with h-BN layer.

quality. The blue shift of the A_{1g} vibrational mode in Raman spectroscopy can be explained as predominately van der Waals interaction between the MoS_2 and the monolayer h-BN or reduction to the electron density. This latter is in accordance with the photoluminescence, where the intensities indicate a probable n-doping effect of MoS_2 in contact with Al_2O_3 encapsulation. This is confirmed by electrical measurements, where a visible n-doping shift after the encapsulation is present. FETs with h-BN layers do not show such an evident shift. The positive effect of an interfacial h-BN layer has been confirmed by ab initio density functional theory calculations and charge transfer analysis, which are in good agreement with the experimental behavior. The electrical performance of the corresponding transistors with h-BN remains reliable and shows lower threshold voltage shifts, lower hysteresis, and lower SS after the Al_2O_3 passivation layer with respect to reference devices without h-BN. Moreover, we have demonstrated high electrical hysteresis stability by maintaining a low hysteresis even with slow sweeping time for FETs with h-BN. This demonstrates that the interface between MoS_2 and the surrounding dielectrics is critical for the hysteresis and stability of MoS_2-based FETs. The demonstrated high interface quality is a key parameter to increase the reliability of MoS_2-based transistor for future integration in electronic circuits.

4. Experimental Section

Device Fabrication: FETs in local back gate configuration have been fabricated using contact photolithography on the top of p-doped Si substrate with 90 nm of SiO_2 thermally grown. Thirty nanometers of Ni was sputtered followed by lift-off to form the back gate electrode. The deposition of 25 nm Al_2O_3 as gate dielectric was performed by thermal ALD at 200 °C using water and trimethylaluminum as precursors. After opening the gate vias, the material stack (MBN-FETs) was transferred using the wet transfer method described in the following paragraph. In parallel, a sample without h-BN (M-FETs) was fabricated as a reference. Nickel edge contacts were created with a sputtering and lift-off process,[52] followed by a dry etching process to pattern the channel material. Channel dimensions are 70 μm width and length between 2 and 5 μm. As a final encapsulation of the devices, 35 nm of Al_2O_3 was deposited with the same thermal ALD as before process after 1 h of annealing step at 300 °C.

Preparation of h-BN/MoS_2/h-BN Stack: The vertical Van der Waals stack was fabricated with multiple wet transfers. The materials of the stack were a commercial monolayer CVD h-BN grown on copper foil and a monolayer MOCVD MoS_2 grown on a sapphire substrate.[53] All 2D materials were spin-coated with poly-methyl-methacrylate (PMMA) as a mechanical resistant transport layer before the transfer. Initially, we etched the copper foil of h-BN in a solution of hydrochloric acid (HCl) and hydrogen peroxide (H_2O_2). h-BN was transferred by scooping it from the water on the prepatterned substrate descried in the previous paragraph. After the complete drying of the sample for 1 day in ambient atmosphere and for 30 min on a hot plate at 180 °C, PMMA was removed in heated acetone. Then, we lifted the MoS_2 monolayer from the sapphire substrate in a potassium hydroxide (KOH) solution and transferred on the top of h-BN on the target substrate. Once the sample was dried and the PMMA was dissolved in heated acetone, the third layer of h-BN was transferred on the top of the stack following the same procedure as described for the first h-BN layer. In parallel, devices with only MOCVD MoS_2 were fabricated using the same wet-transfer technique.

Device Characterization: Raman and PL measurements were conducted using a WITec confocal Raman microscope equipped with a 532 nm laser. Both measurements were performed at room temperature on an area of 2 × 50 μm in 200 different points with a laser power of 1 mW. Resolutions for PL and Raman were 300 g mm^{-1} grating and 1800g mm^{-1}, respectively. The graphs were obtained by averaging the PL and Raman spectra measured in the 200 points. Electrical characterization of MoS_2 FETs consisted of measurement of I_d–V_g characteristics. The measurements were performed using a Keithley SCS4200 parameter analyzer and a Lakeshore probe station either in a vacuum (3×10^{-5} mBar) or in an ambient condition (42% humidity) in complete darkness and at room temperature (21 °C).

Computational Methods: First principles density functional theory simulations have been performed using Quantum Espresso package.[50] For the self-consistent calculation a gradient-corrected exchange correlation functional (Perdew–Burke–Ernzerhof)[54] and PAW pseudopotentials had been used,[55] setting an energy cut-off of 80 Ry for the wave functions of the basis set while a cut-off of 800 Ry for the electron density. A 3 × 3 × 1 Monkhorst–Pack Γ-centered grid was employed, taking into account van der Waals interactions through nonlocal vdW-DF-OBK8 exchange-correlation functional.[56–59] The optimized distances d_0, between the two Al_2O_3 layers, and d_{hBN}, between h-BN and MoS_2, have been obtained varying the distances with a step of 0.05 Å, with Γ point calculations considering an energy cut-off of 60 and 300 Ry for the wave functions and the electron density, respectively. For quantifying the charge transfer, this work had used the Bader formalism using a 180 × 180 × 576 mesh for the Al_2O_3/MoS_2/Al_2O_3 structure while a 180 × 180 × 720 mesh for the Al_2O_3/h-BN/MoS_2/h-BN/Al_2O_3 structure.[51]

Supporting Information

Supporting Information is available from the Wiley Online Library or from the author.

Acknowledgements

The authors acknowledge the support by the European Union's Horizon 2020 research and innovation program under the grant agreements Graphene Flagship (881603), QUEFORMAL (829035), 2D-EPL (952792) and ORIGENAL (863258), the German Research Foundation DFG under the projects MOSTFLEX (LE 2440/7-1; WA 4139/3-1) and ULTIMOS2 (LE 2440/8-1), the German Ministry of Education BMBF under the projects NEUROTEC (16ES1134) and NEUROTEC II (16ME0399, 16ME0400), and the Italian Ministry of Education, University and Research (MIUR) in the framework of the CrossLab Department of Excellence project.

Open access funding enabled and organized by Projekt DEAL.

Conflict of Interest

The authors declare no conflict of interest.

Data Availability Statement

The data that support the findings of this study are available from the corresponding author upon reasonable request.

Keywords

Al_2O_3, fixed charges, h-BN encapsulation, hysteresis in MoS_2-based devices, MoS_2 transistors

Received: February 1, 2022
Revised: March 25, 2022
Published online:

[1] H. Zhang, H. Wang, *Advanced Nanoelectronics*, John Wiley & Sons, Ltd, Hoboken, NJ, USA **2018**, pp. 55–90.
[2] K. S. Novoselov, A. K. Geim, S. V. Morozov, D. Jiang, Y. Zhang, S. V. Dubonos, I. V. Grigorieva, A. A. Firsov, *Science* **2004**, *306*, 666.
[3] M. C. Lemme, T. J. Echtermeyer, M. Baus, H. Kurz, *IEEE Electron Device Lett.* **2007**, *28*, 282.
[4] Q. H. Wang, K. Kalantar-Zadeh, A. Kis, J. N. Coleman, M. S. Strano, *Nat. Nanotechnol.* **2012**, *7*, 699.
[5] D. Jariwala, V. K. Sangwan, L. J. Lauhon, T. J. Marks, M. C. Hersam, *ACS Nano* **2014**, *8*, 1102.
[6] L. Li, Y. Yu, G. J. Ye, Q. Ge, X. Ou, H. Wu, D. Feng, X. H. Chen, Y. Zhang, *Nat. Nanotechnol.* **2014**, *9*, 372.
[7] M. Schmidt, M. C. Lemme, H. D. B. Gottlob, F. Driussi, L. Selmi, H. Kurz, *Solid-State Electron.* **2009**, *53*, 1246.
[8] B. Radisavljevic, A. Radenovic, J. Brivio, V. Giacometti, A. Kis, *Nat. Nanotechnol.* **2011**, *6*, 147.
[9] Y. Yoon, K. Ganapathi, S. Salahuddin, *Nano Lett.* **2011**, *11*, 3768.
[10] D. Lembke, S. Bertolazzi, A. Kis, *Acc. Chem. Res.* **2015**, *48*, 100.
[11] Y. Yu, Illarionov, K. K. H. Smithe, M. Waltl, T. Knobloch, E. Pop, T. Grasser, *IEEE Electron Device Lett.* **2017**, *38*, 1763.
[12] X. Wang, T.-B. Zhang, W. Yang, H. Zhu, L. Chen, Q.-Q. Sun, D. W. Zhang, *Appl. Phys. Lett.* **2017**, *110*, 053110.
[13] C. D. English, G. Shine, V. E. Dorgan, K. C. Saraswat, E. Pop, *Nano Lett.* **2016**, *16*, 3824.
[14] Q. Qian, B. Li, M. Hua, Z. Zhang, F. Lan, Y. Xu, R. Yan, K. J. Chen, *Sci. Rep.* **2016**, *6*, 27676.
[15] Y. Y. Illarionov, T. Knobloch, M. Jech, M. Lanza, D. Akinwande, M. I. Vexler, T. Mueller, M. C. Lemme, G. Fiori, F. Schwierz, T. Grasser, *Nat. Commun.* **2020**, *11*, 3385.
[16] Q. A. Vu, S. Fan, S. H. Lee, M.-K. Joo, W. J. Yu, Y. H. Lee, *2D Mater.* **2018**, *5*, 031001.
[17] J. Zou, L. Wang, F. Chen, *AIP Adv.* **2019**, *9*, 095061.
[18] Y. Y. Illarionov, A. G. Banshchikov, D. K. Polyushkin, S. Wachter, T. Knobloch, M. Thesberg, L. Mennel, M. Paur, M. Stöger-Pollach, A. Steiger-Thirsfeld, M. I. Vexler, M. Waltl, N. S. Sokolov, T. Mueller, T. Grasser, *Nat. Electron.* **2019**, *2*, 230.
[19] D. J. Late, B. Liu, H. S. S. R. Matte, V. P. Dravid, C. N. R. Rao, *ACS Nano* **2012**, *6*, 5635.
[20] Y.-C. Kung, N. Hosseini, D. Dumcenco, G. E. Fantner, A. Kis, *Adv. Electron. Mater.* **2019**, *5*, 1800492.
[21] N. Liu, J. Baek, S. M. Kim, S. Hong, Y. K. Hong, Y. S. Kim, H.-S. Kim, S. Kim, J. Park, *ACS Appl. Mater. Interfaces* **2017**, *9*, 42943.
[22] S. J. Yun, Y.-W. Ko, J. W. Lim, *Appl. Phys. Lett.* **2004**, *85*, 4896.
[23] J. Meyer, P. Görrn, F. Bertram, S. Hamwi, T. Winkler, H.-H. Johannes, T. Weimann, P. Hinze, T. Riedl, W. Kowalsky, *Adv. Mater.* **2009**, *21*, 1845.
[24] T. Li, B. Wan, G. Du, B. Zhang, Z. Zeng, *AIP Adv.* **2015**, *8*, 057102.
[25] S. Y. Kim, S. Park, W. Choi, *Appl. Phys. Lett.* **2016**, *109*, 152101.
[26] J. Na, M.-K. Joo, M. Shin, J. Huh, J.-S. Kim, M. Piao, J.-E. Jin, H.-K. Jang, H. J. Choi, J. H. Shim, G.-T. Kim, **2014**, *6*, 433.
[27] H. Liu, P. D. Ye, *IEEE Electron Device Lett.* **2012**, *33*, 546.
[28] G.-H. Lee, X. Cui, Y. D. Kim, G. Arefe, X. Zhang, C.-H. Lee, F. Ye, K. Watanabe, T. Taniguchi, P. Kim, J. Hone, *ACS Nano* **2015**, *9*, 7019.
[29] X. Han, J. Lin, J. Liu, N. Wang, D. Pan, *J. Phys. Chem. C* **2019**, *123*, 14797.
[30] C. Lee, S. Rathi, M. A. Khan, D. Lim, Y. Kim, S. J. Yun, D. Youn, K. Watanabe, T. Taniguchi, G.-H. Kim, *Nanotechnology* **2018**, *9*, 335202.
[31] A. Saito, T. Ayano, S. Nomura, *Jpn. J. Appl. Phys.* **2018**, *57*, 045201.
[32] Y. Y. Illarionov, T. Knobloch, T. Grasser, *Solid-State Electron.* **2021**, *185*, 108043.
[33] Y. Liu, H. Wu, H.-C. Cheng, S. Yang, E. Zhu, Q. He, M. Ding, D. Li, J. Guo, N. O. Weiss, Y. Huang, X. Duan, *Nano Lett.* **2015**, *15*, 3030.
[34] Y. Y. Illarionov, T. Knobloch, T. Grasser, *Solid-State Electron.* **2021**, *185*, 108043.
[35] T. Knobloch, Y. Y. Illarionov, F. Ducry, C. Schleich, S. Wachter, K. Watanabe, T. Taniguchi, T. Mueller, M. Waltl, M. Lanza, M. I. Vexler, M. Luisier, T. Grasser, *Nat. Electron.* **2021**, *4*, 98.
[36] X. Zou, C.-W. Huang, L. Wang, L.-J. Yin, W. Li, J. Wang, B. Wu, Y. Liu, Q. Yao, C. Jiang, W.-W. Wu, L. He, S. Chen, J. C. Ho, L. Liao, *Adv. Mater.* **2016**, *28*, 2062.
[37] M. Xu, T. Xu, A. Yu, H. Wang, H. Wang, M. Zubair, M. Luo, C. Shan, X. Guo, F. Wang, W. Hu, Y. Zhu, *Adv. Opt. Mater.* **2021**, *9*, 2100937.
[38] C. Lee, H. Yan, L. E. Brus, T. F. Heinz, J. Hone, S. Ryu, *ACS Nano* **2010**, *4*, 2695.
[39] H. Li, Q. Zhang, C. C. R. Yap, B. K. Tay, T. H. T. Edwin, A. Olivier, D. Baillargeat, *Adv. Funct. Mater.* **2012**, *22*, 1385.
[40] B. Huang, M. Zheng, Y. Zhao, J. Wu, J. T. L. Thong, *ACS Appl. Mater. Interfaces* **2019**, *11*, 35438.
[41] L. Li, I. Lee, D. Lim, M. Kang, G.-H. Kim, N. Aoki, Y. Ochiai, K. Watanabe, T. Taniguchi, *Nanotechnology* **2015**, *26*, 295702.
[42] A. K. Singh, R. G. Hennig, A. V. Davydov, F. Tavazza, *Appl. Phys. Lett.* **2015**, *107*, 053106.
[43] S. Park, S. Y. Kim, Y. Choi, M. Kim, H. Shin, J. Kim, W. Choi, *ACS Appl. Mater. Interfaces* **2016**, *8*, 11189.
[44] N. Mao, Y. Chen, D. Liu, J. Zhang, L. Xie, *Small* **2013**, *9*, 1312.

[45] M. Buscema, G. A. Steele, H. S. J. van der Zant, A. Castellanos-Gomez, *Nano Res.* **2014**, *7*, 561.
[46] J. Zhang, L. Ding, S. Zhou, Y. M. Xiao, W. Xu, *Phys. Status Solidi RRL* **2020**, *14*, 2000222.
[47] B. Chakraborty, A. Bera, D. V. S. Muthu, S. Bhowmick, U. V. Waghmare, A. K. Sood, *Phys. Rev. B* **2012**, *85*, 161403.
[48] S. Mouri, Y. Miyauchi, K. Matsuda, *Nano Lett.* **2013**, *13*, 5944.
[49] S. Y. Kim, H. I. Yang, W. Choi, *Appl. Phys. Lett.* **2018**, *113*, 133104.
[50] P. Giannozzi, S. Baroni, N. Bonini, M. Calandra, R. Car, C. Cavazzoni, D. Ceresoli, G. L. Chiarotti, M. Cococcioni, I. Dabo, A. Dal Corso, S. de Gironcoli, S. Fabris, G. Fratesi, R. Gebauer, U. Gerstmann, C. Gougoussis, A. Kokalj, M. Lazzeri, L. Martin-Samos, N. Marzari, F. Mauri, R. Mazzarello, S. Paolini, A. Pasquarello, L. Paulatto, C. Sbraccia, S. Scandolo, G. Sclauzero, A. P. Seitsonen, *J. Phys.: Condens. Matter* **2009**, *21*, 395502.
[51] W. Tang, E. Sanville, G. Henkelman, *J. Phys.: Condens. Matter* **2009**, *21*, 084204.
[52] M. Shaygan, M. Otto, A. A. Sagade, C. A. Chavarin, G. Bacher, W. Mertin, D. Neumaier, *Ann. Phys.* **2017**, *529*, 1600410.
[53] H. Cun, M. Macha, H. Kim, K. Liu, Y. Zhao, T. LaGrange, A. Kis, A. Radenovic, *Nano Res.* **2019**, *12*, 2646.
[54] J. P. Perdew, K. Burke, M. Ernzerhof, *Phys. Rev. Lett.* **1996**, *77*, 3865.
[55] D. Vanderbilt, *Phys. Rev. B* **1990**, *41*, 7892.
[56] T. Thonhauser, S. Zuluaga, C. A. Arter, K. Berland, E. Schröder, P. Hyldgaard, *Phys. Rev. Lett.* **2015**, *115*, 136402.
[57] T. Thonhauser, V. R. Cooper, S. Li, A. Puzder, P. Hyldgaard, D. C. Langreth, *Phys. Rev. B* **2007**, *76*, 125112.
[58] K. Berland, V. R. Cooper, K. Lee, E. Schröder, T. Thonhauser, P. Hyldgaard, B. I. Lundqvist, *Rep. Prog. Phys.* **2015**, *78*, 066501.
[59] D. C. Langreth, B. I. Lundqvist, S. D. Chakarova-Käck, V. R. Cooper, M. Dion, P. Hyldgaard, A. Kelkkanen, J. Kleis, L. Kong, S. Li, P. G. Moses, E. Murray, A. Puzder, H. Rydberg, E. Schröder, T. Thonhauser, *J. Phys.: Condens. Matter* **2009**, *21*, 084203.